

A Novel Dendrite-Free $\text{Mn}^{2+}/\text{Zn}^{2+}$ Hybrid Battery with 2.3 V Voltage Window and 11000-Cycle Lifespan

Ming Li, Qiu He, Zilan Li, Qi Li,* Yuxin Zhang, Jiashen Meng, Xiong Liu, Shidong Li, Buke Wu, Lineng Chen, Ziang Liu, Wen Luo, Chunhua Han,* and Liqiang Mai*

With the increasing energy crisis and environmental pollution, rechargeable aqueous Zn-based batteries (AZBs) are receiving unprecedented attention due to their list of merits, such as low cost, high safety, and nontoxicity. However, the limited voltage window, Zn dendrites, and relatively low specific capacity are still great challenges. In this work, a new reaction mechanism of reversible Mn^{2+} ion oxidation deposition is introduced to AZBs. The assembled $\text{Mn}^{2+}/\text{Zn}^{2+}$ hybrid battery ($\text{Mn}^{2+}/\text{Zn}^{2+}$ HB) based on a hybrid storage mechanism including Mn^{2+} ion deposition, Zn^{2+} ion insertion, and conversion reaction of MnO_2 can achieve an ultrawide voltage window (0–2.3 V) and high capacity (0.96 mAh cm^{-2}). Furthermore, the carbon nanotubes coated Zn anode is proved to effectively inhibit Zn dendrites and control side reaction, hence exhibiting an ultrastable cycling (33 times longer than bare Zn foil) without obvious polarization. Benefiting from the optimal Zn anode and highly reversible $\text{Mn}^{2+}/\text{Zn}^{2+}$ hybrid storage mechanism, the $\text{Mn}^{2+}/\text{Zn}^{2+}$ HB shows an excellent cycling performance over 11 000 cycles with a 100% capacity retention. To the best of the authors' knowledge, it is the highest reported cycling performance and wide voltage window for AZBs with mild electrolyte, which may inspire a great insight into designing high-performance aqueous batteries.

1. Introduction

With the consumption of fossil fuels and the ever-growing demands for renewable clean energy, it is highly desired to develop high-performance energy storage/conversion systems with high capacity, long lifespan, low cost, and environmental friendliness.^[1] Nowadays, the commercial lithium ion batteries have been widely applied in many fields due to their high energy densities. However, a series of intrinsic drawbacks including poor safety, environmental pollution derived from organic electrolytes as well as high cost from the scarce lithium resources remain challenges and hinder their

further development.^[2] Hence, exploring novel approaches to achieve more efficient energy storage is highly demanded. Recently, aqueous batteries are attracting unprecedented attention particularly owing to their high safety, high ion conductivity, low cost, and environmental friendliness.^[3] To date, numerous aqueous batteries based on Li^+ , Na^+ , K^+ , Mg^{2+} , Ca^{2+} , Zn^{2+} , Al^{3+} , Fe^{3+} , and/or mixed metal ions as charge carriers have been reported,^[4] which find potential applications in fields such as grid-scale energy storage, wearable devices, and etc.^[5]

Among them, as a promising candidate, the rechargeable aqueous Zn-based batteries (AZBs) including Zn-ion batteries (mild electrolyte),^[6] Zn–Co/Ag/Ni alkaline batteries^[7] and Zn–air batteries in alkaline electrolyte^[8] have been extensively studied due to their unparalleled advantages of Zn anode. In general, metal Zn has the features of high theoretical capacity (820 mAh g^{-1}), high electrical conductivity, nontoxicity, easy

processing, and suitable redox potential (-0.76 V vs standard hydrogen electrode).^[9] However, most of AZBs reported so far have encountered the same challenges, which are the narrow voltage window, unsatisfactory capacity, and poor cycling performance.^[10] For example, all Zn-ion batteries operated in mild electrolyte including Zn//V-based, Zn//Mn-based, and Zn//Prussian blue analogs-based hold a narrow voltage window of 0.3–1.6, 0.9–1.8, and 0.2–1.8 V, respectively.^[11] Even though AZBs in alkaline electrolyte display a higher voltage than that achieved in mild medium, their voltage windows are still only about 1.2–1.9 V.^[12] Meanwhile, the alkaline electrolytes show stronger corrosion than mild neutral electrolytes, which greatly limit their wide applications. Moreover, the unstable cycling performance in AZBs due to the Zn dendrites and side reaction on the surface of Zn anode is also unsatisfactory.^[10] To date, the electrolyte optimization or structural design are the common ways to suppress the growth of Zn dendrite and improve the cycling stability. For example, Chen and co-workers reported that aqueous electrolyte $\text{Zn}(\text{CF}_3\text{SO}_3)_2$ can suppress the formation of detrimental dendrites in AZBs owing to the better reversibility and faster kinetics of Zn deposition/dissolution than that in ZnSO_4 electrolyte.^[13] However, $\text{Zn}(\text{CF}_3\text{SO}_3)_2$ is too expensive ($\approx \$ 8.1 \text{ g}^{-1}$, prices from Sigma-Aldrich) to be applied

M. Li, Q. He, Z. L. Li, Prof. Q. Li, Y. X. Zhang, J. S. Meng, X. Liu, S. D. Li, B. K. Wu, L. N. Chen, Z. A. Liu, Dr. W. Luo, Prof. C. H. Han, Prof. L. Q. Mai
State Key Laboratory of Advanced Technology for Materials Synthesis and Processing

Wuhan University of Technology
Hubei, Wuhan 430070, P. R. China
E-mail: qi.li@whut.edu.cn; mlq518@whut.edu.cn; hch5927@whut.edu.cn

The ORCID identification number(s) for the author(s) of this article can be found under <https://doi.org/10.1002/aenm.201901469>.

DOI: 10.1002/aenm.201901469

in real energy storage systems.^[14] Researchers have also proposed to suppress the growth of dendrites by constructing Zn anodes with a 3D structure.^[15] However, its complex production processes and high production costs limit their wide applications. Therefore, exploring a simple, low-cost and effective way to assemble high-performance AZBs with a wide voltage and stable Zn anode is still a great challenge.

Herein, inspired by the new Mn–H battery reported by Cui and co-workers,^[16] we propose and demonstrate a low-cost Mn²⁺/Zn²⁺ hybrid battery (Mn²⁺/Zn²⁺ HB) based on a new-type hybrid storage mechanism including Mn²⁺/MnO₂ reversible deposition/dissolution, Zn²⁺ insertion, and chemical conversion reaction (between MnO₂ and MnOOH). In particular, by introducing a novel mechanism based on deposition/dissolution reactions between soluble Mn²⁺ and solid MnO₂ in electrolyte, a wide voltage window of 2.3 V and excellent specific capacity of 0.96 mAh cm⁻² can be achieved. Moreover, it is worth noting that the MnO₂ cathode is synthesized by simply soaking the low-cost polyester cloth into carbon nanotubes (CNTs) ink followed by an in situ self-sacrificing reaction. While a simple method is applied to obtain the antidendrite CNT-coated Zn anode, leading to significantly improved stability of Zn foil for over 400 h cycling without obvious polarization. Benefiting from the highly reversible deposition/dissolution mechanism in the MnO₂ cathode and the stable Zn anode, the Mn²⁺/Zn²⁺ hybrid battery exhibits ultrastable cycle performance of over 11 000 cycles without decay as well as almost 100% Coulombic efficiency. This work provides a new way to improve battery capacity and cycling performance through electrolyte regulation and dendritic inhibition. It heralds a new opportunity in the development of high performance, low-cost, safe aqueous batteries.

2. Results and Discussion

2.1. Morphology and Structure Characterization

The integrated flexible MnO₂ cathode and CNTs modified Zn anode are fabricated and schematically depicted in **Figure 1**.

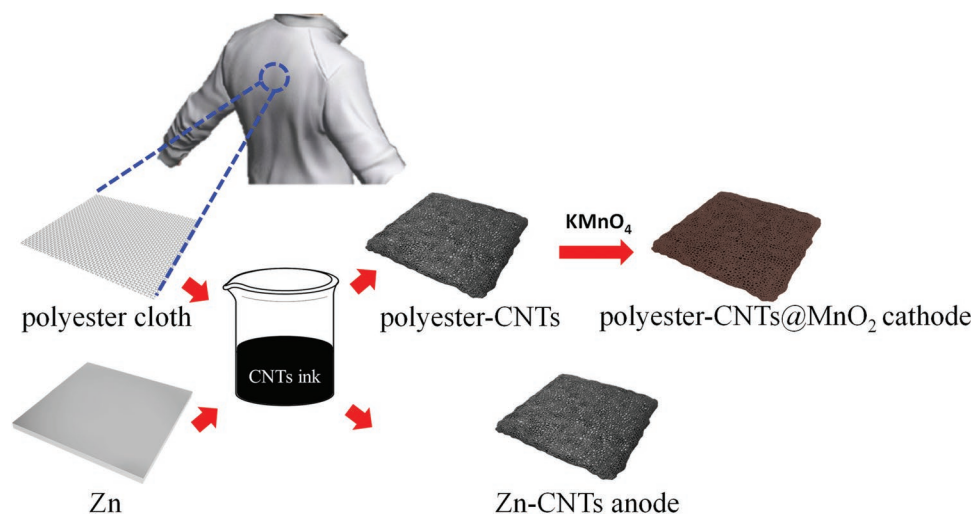


Figure 1. Schematic illustration of the Mn²⁺/Zn²⁺ HB using the elaborate Zn-CNTs anode and polyester-CNTs@MnO₂ cathode.

First, the insulating polyester cloth (Figure S1a–c, Supporting Information) is converted to the flexible conductive substrate (polyester-CNTs) by soaking into CNTs ink and drying (Figure S1d–i, Supporting Information). Here, polyvinyl pyrrolidone (PVP) is added as a surfactant to avoid agglomeration of CNTs on polyester fiber (Figure S2, Supporting Information). As a result, the polyester-CNTs exhibits a much smaller resistance than original polyester cloth due to the highly conductive CNTs coating (Figure S3, Supporting Information). Finally, MnO₂ in situ grows on CNTs surface to obtain the binder-free integrated flexible electrode (polyester-CNTs@MnO₂) after the reaction between CNTs and KMnO₄ (**Figure 2a–d**). The obtained polyester-CNTs@MnO₂ shows a high strength of 60 MPa (the carbon cloth is only 3.5 MPa) and superior stability under the ultrasonic treatment (Figure 2e,f). In particular, the polyester cloth is as cheap as only \$ 0.4 for the size of 1000 cm × 900 cm compared with expensive carbon cloth (about \$ 145 for 40 cm × 40 cm, Ce Tech Co., Ltd), which indicates a sharp drop in production cost. On the other hand, the dendrite-free CNTs coated Zn foil (Zn-CNTs) was prepared by the same dipping method. Importantly, the introduction of alcohol contributes to a higher interfacial tension and slow gas release in mixed solvent of CNTs ink, thus effectively preventing the generation of bubbles on the surface of Zn foil during the drying process (Figure S4, Supporting Information).^[17] Moreover, both Zn-CNTs and polyester-CNTs@MnO₂ electrodes show the enhanced wettability after CNTs coating and growth of MnO₂, which facilitates the penetration of the electrolyte (Figure S5, Supporting Information).

The transmission electron microscope (TEM) images show the uniform morphology of CNTs with inner/outer diameters of 7/20 nm, respectively (Figure S6, Supporting Information). The corresponding selected area electron diffraction (SAED) pattern reveals characteristic planes of (002), (100), and (110) for graphite, which is consistent with previous reports.^[18] Energy dispersive X-ray spectroscopy (EDS) mapping results indicate the major content of C and small amount of O element. As shown in Figure 2g,h, the well-maintained hollow structure of CNTs with MnO₂ can be observed when

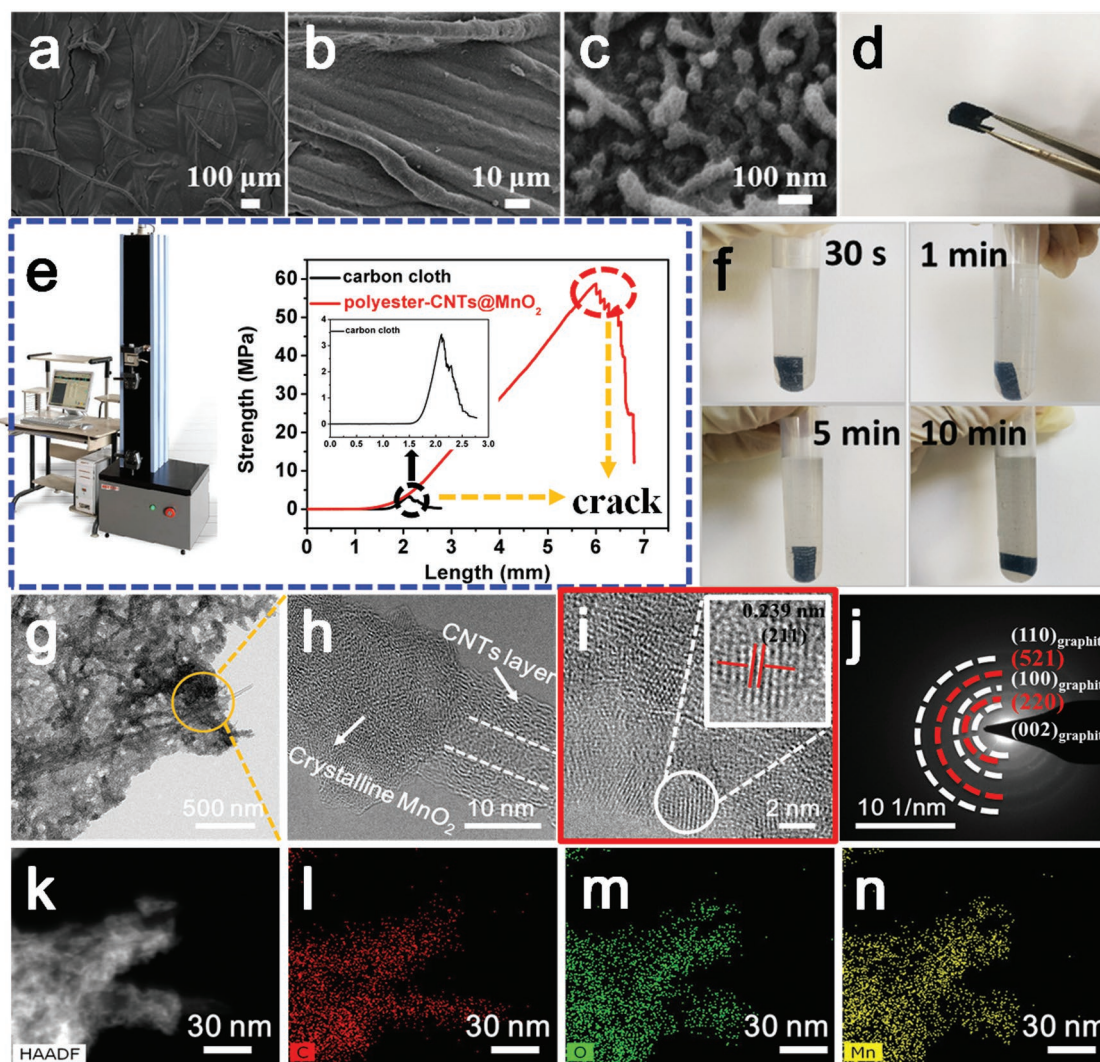


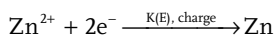
Figure 2. a–c) SEM images of polyester-CNTs@MnO₂ electrode. d) The optical image, e) tensile strength test of flexible polyester-CNTs@MnO₂ electrode. f) The stability test under ultrasonic condition at different time. g–j) TEM, HRTEM, and SAED images, and k–n) corresponding EDS mapping images of polyester-CNTs@MnO₂.

reaction condition was set to 1.5 h at 120 °C compared with other reaction time (Figure S7, Supporting Information). The high-resolution transmission electron microscopy (HRTEM) image shows that *d*-spacing from the lattice fringes is about 0.239 nm, matching well with the (211) plane of α -MnO₂ (Figure 2i). The SAED result of the MnO₂ area indicates that the ring patterns are well indexed to the (521) and (220) planes of MnO₂ (Figure 2j). The corresponding EDS mapping results of polyester-CNTs@MnO₂ exhibit obvious C, O, and Mn elements (Figure 2k–n). The crystal structures of the prepared polyester-CNTs@MnO₂ were also characterized by X-ray diffraction (XRD). In Figure S8a (Supporting Information), all the characteristic peaks agree well with the standard card of tunnel α -MnO₂ (No. 44–0141 crystal system: tetragonal, with the space group of I4/m, space group number of 87; *a* = 9.78 Å, *b* = 9.78 Å, *c* = 2.86 Å, $\alpha = \beta = \gamma = 90^\circ$) and all tunnels are built by corner-shared double chains consisted of MnO₆ octahedral (Figure S8b, Supporting Information). Compared

with polyester-CNTs, the obvious peaks located at 499 and 564 cm⁻¹ in the Raman spectrum of polyester-CNTs@MnO₂ are well consistent with stretching modes of Mn–O^[19] (Figure S8c, Supporting Information). Moreover, the weakened D (disordered carbon) and G (graphitic carbon) peaks in polyester-CNTs@MnO₂ compared to the polyester-CNTs are observed, reflecting the successful reaction of CNTs with KMnO₄. In Figure S8d (Supporting Information), full X-ray photoelectron spectroscopy (XPS) results shows the characteristic peaks of O, N, Mn, C. The Mn 2p_{3/2} and Mn 2p_{1/2} peaks are located at 642.2 and 653.9 eV with an energy separation of 11.7 eV, which are in good agreement with the results reported for MnO₂ (Figure S8e, Supporting Information).^[20] The deconvoluted O 1s spectrum can be fitted with three components that are associated with the Mn–O–Mn bond (529.7 eV), Mn–OH bond (531.2 eV), and H–O–H bond (532.6 eV), which is consistent with the reported MnO₂ (Figure S8f, Supporting Information).^[16]

2.2. Antidendrite Properties of Zn-CNTs Anode

In order to evaluate the effect of CNTs protective layer on the stability of Zn anode, CR 2016 coin-type cells were assembled, 2 M ZnSO₄ and 1 M MnSO₄ mixed solution was used as electrolyte. The galvanostatic cycling performance of Zn symmetrical cells with bare Zn foil (black lines) or CNTs coated Zn (red lines) electrodes were tested at 0.5 mA cm⁻². The Zn-CNTs||Zn-CNTs symmetrical battery exhibits a small original polarization, which is equal with bare Zn foil at the first cycle (Figure S9a,b, Supporting Information). It can be attributed to the similar electrochemical impedance spectroscopy (EIS) results between Zn||Zn symmetrical battery ($R_s = 18.3 \Omega$, $R_{ct} = 51.4 \Omega$, $Z_w = 7.17 \Omega$) and Zn-CNTs||Zn-CNTs symmetrical battery ($R_s = 17.63 \Omega$, $R_{ct} = 56.56 \Omega$, $Z_w = 22.5 \Omega$) in Figure S9c in the Supporting Information. However, under the high current density of 0.5 mA cm⁻², the symmetrical battery with bare Zn foil show the unstable cycle performance and the significantly increased polarization from 80 to 210 mV over just a few cycles. After only 12 h cycle test, a sudden and profound polarization increase (≈ 2.4 V) was detected for the bare Zn||Zn symmetrical battery. On the contrary, the Zn-CNTs||Zn-CNTs symmetrical battery is much more stable and shows the stable cycling without obvious polarization for more than 400 h which are 33 times longer than the Zn||Zn symmetrical battery (Figure S9d, Supporting Information). Figure S10 (Supporting Information) shows the surface morphologies of Zn foil with different cycle numbers, displaying the obvious dendrite formation. To better understand the formation and suppression mechanism of Zn dendrites, the schematic illustrations are described in Figure 3a. In fact, the dendrite is controlled by reaction as



where $K(E) = K^0 \exp[-\alpha n_e F (E^0 - E)/RT]$, α is the transfer coefficient, n_e is the number of transferred electrons, F is the Faraday constant, R is the gas constant.^[21] Herein, $K(E)$ determines the kinetics of Zn deposition on the surface of Zn foil, which is controlled by temperature (T) and overpotential ($E^0 - E$). Owing to the anisotropic deposition process of Zn during the charge process, the Zn nuclei with high overpotential appears on the surface of the Zn foil and further develop into dendrites with the increasing cycles. Benefiting from the charge redistribution effect of CNTs on overpotential, the uniform Zn nanosheet under the CNTs layer on Zn foil surface can be observed without dendrite formation after 400 h experiment (Figure 3b–d).

Moreover, the significant amount of O and S elements on the surface of the Zn foil can be observed after cycling (Figure S10d–f, Supporting Information). The XRD patterns of Zn foil after cycling test are indexed to Zn₄SO₄(OH)₆·4H₂O (3Zn²⁺ + 6OH⁻ + ZnSO₄ + 4H₂O → Zn₄SO₄(OH)₆·4H₂O), indicating the presence of side reaction (Figure S11, Supporting Information). Moreover, a large amount of O and S elements present on the surface of CNTs can be observed. However, the surface of Zn foil only shows Zn element without other impurities (Figure 3b–d). The XRD results further prove a significant reduction of side reactions on Zn foil after CNTs coating. Through the density functional theory (DFT) calculations, the CNTs protective layer containing N and O functional

groups (Figure S12, Supporting Information) shows a higher binding energy of 3.41/3.40 eV with O/S impurity atom than Zn foil of 2.08/1.37 eV, indicating strong oxygenophilic and sulfurophilic properties (Figure 3e–j). This particular atomic adsorption effect of the CNTs layer is illustrated in Figure S13 (Supporting Information). As a result, the adsorption effect of CNTs protective layer can guide the side reaction to occur only on the CNTs protective layer during the cycles, ensuring that the faster kinetics of Zn deposition/dissolution on the Zn foil is not affected by the side reaction. Inspired by these findings, we consider that the CNTs coating plays an important role on controlling Zn dendrites and side reaction. Compared with other strategies such as nanostructure design, the antidendrite Zn anode is simply fabricated, exhibiting low cost, excellent stability improvement.

2.3. Electrochemical Performance of Mn²⁺/Zn²⁺ HB

On the basis of the stable Zn-CNTs anode and binder-free flexible polyester-CNTs@MnO₂ cathode, an aqueous Mn²⁺/Zn²⁺ HB in mild electrolyte was assembled. The Mn²⁺/Zn²⁺ HBs with different electrolyte concentrations were studied to achieve the optimal electrochemical performance. The mixed solution with 2 M ZnSO₄ and 0, 0.2, 0.5, 1, or 2 M MnSO₄ were applied as the electrolytes, respectively. In particular, MnSO₄ is selected as the soluble Mn²⁺ salt due to its low cost, high solubility in water (≈ 4.2 M at room temperature) and good electrochemical stability of SO₄²⁻.^[22] According to the galvanostatic charge–discharge (GCD) curves, the voltage window rose significantly with the increase of concentration of Mn²⁺. When the electrolyte is pure 2 M ZnSO₄ without Mn²⁺ addition, the voltage window is only 2.0 V. With the addition of Mn²⁺ in the electrolyte, the voltage window can be lifted to 2.3 V. A high specific areal capacity of 0.96 mAh cm⁻² and almost 100% of Coulombic efficiency are achieved when the Mn²⁺ ion concentration in electrolyte is 1 M. As further increasing the Mn²⁺ ion concentration to 2 M, the Mn²⁺/Zn²⁺ HB can achieve a higher capacity of 1.0 mAh cm⁻² but with a low Coulombic efficiency of 63.9% (Figure S14, Supporting Information). Hence, the mild solution of 2 M ZnSO₄ + 1 M MnSO₄ was used as the optimal electrolyte in Mn²⁺/Zn²⁺ HB.

The electrochemical stability window with different concentrations of electrolytes is evaluated using linear cyclic voltammetry (LSV) test. The Mn²⁺/Zn²⁺ HB starts to produce oxygen due to water splitting at 2.32 V (vs Zn/Zn²⁺) in the mixed aqueous electrolyte, which is significantly higher than that in the alkaline medium or pure ZnSO₄ (1.93 V) (Figure S15, Supporting Information). Thus, the electrochemical window of Mn²⁺/Zn²⁺ HB can be expected to extend up to 2.3 V, which is supported by the GCD curve in Figure 4a. Moreover, the almost 100% Coulombic efficiency also proved that there is no water oxidation occurring. The wide voltage window of 2.3 V is higher than all other AZBs and most of aqueous batteries based on mild electrolytes that have been reported (Table S1, Supporting Information), as far as we know. The cyclic voltammetry (CV) curves in Figure 4b show the typical peaks (reduction peaks of 1.25 and 1.4 V, oxidation peak of 1.6 V) at a low scan rate of 0.1 mV s⁻¹, which are consistent with the reported insertion and extraction mechanism of Zn²⁺ ions into α -MnO₂.^[23] With the

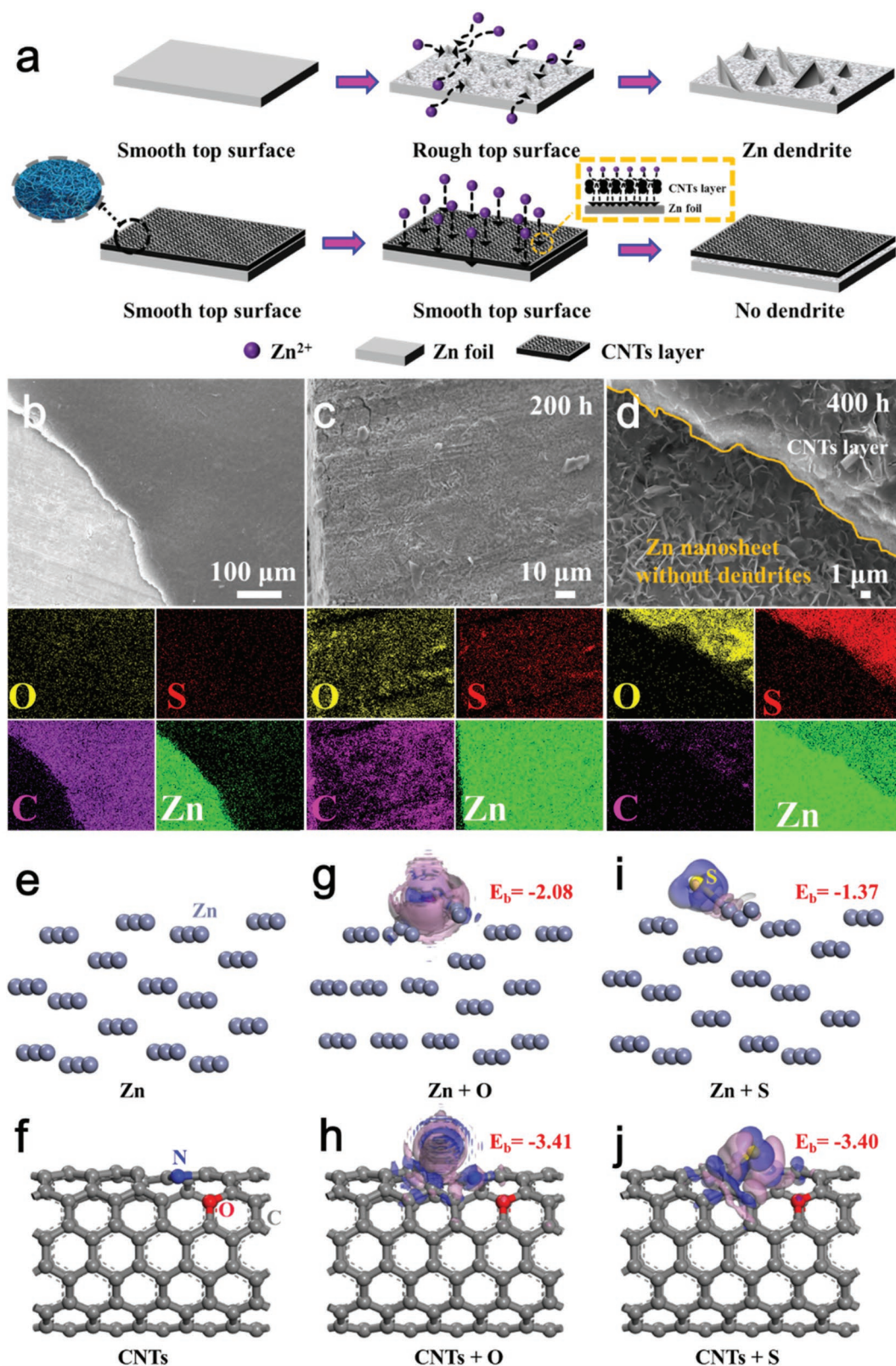


Figure 3. a) Schematic illustrations of morphology evolution/antidendrite mechanism for bare and CNTs coated Zn foils during cycling process. b–d) SEM and corresponding EDS mapping images of the Zn–CNTs during cycling process. The stabilized structures of e) Zn (202) surface and f) CNTs. The optimized configurations of Zn planes adsorbing g) O and i) S. The optimized configurations of CNTs adsorbing h) O and j) S. The semiluculent bubbles in structures of insets (g–j) refer to charge density differences, in which the pink bubbles represent the electronic decrease and the blue represent the electronic increase (the isosurface value is $\pm 0.02 e \text{ bohr}^{-3}$).

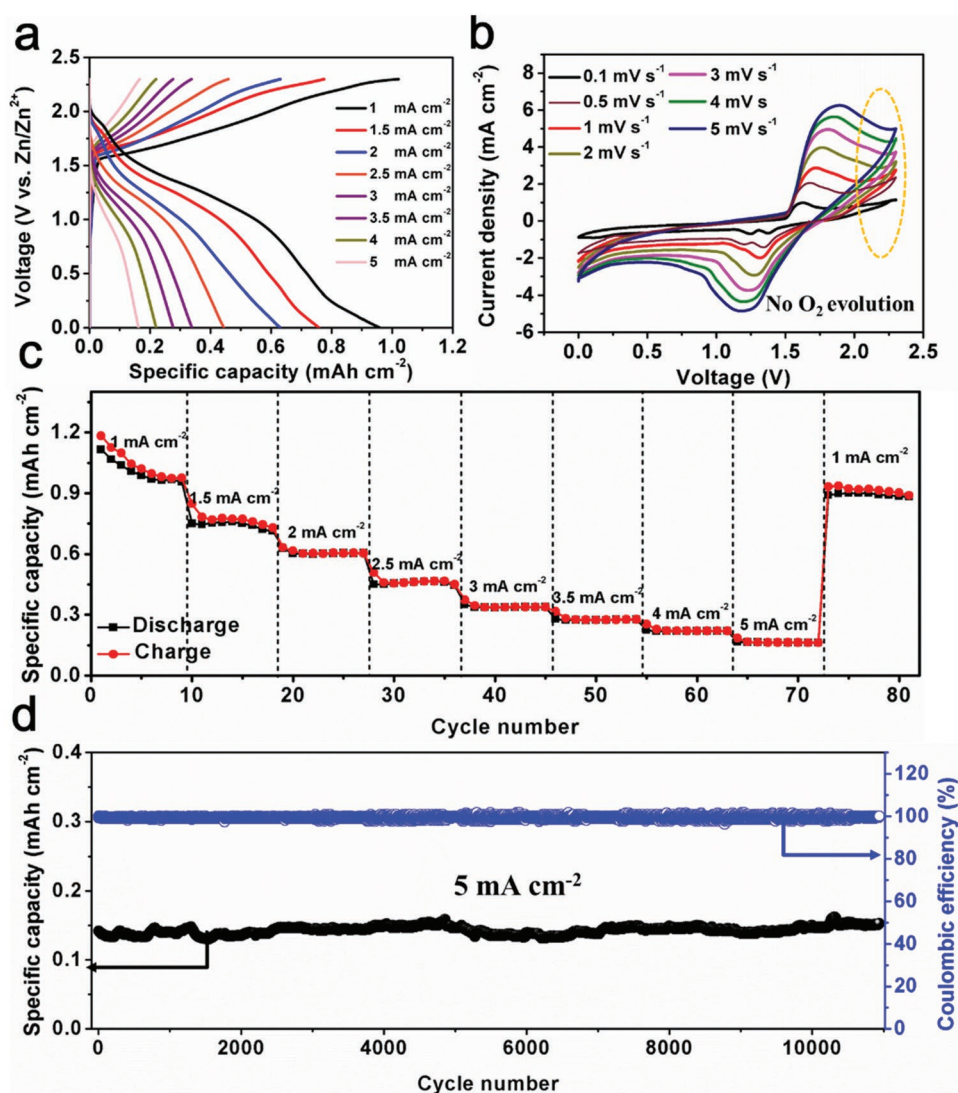


Figure 4. Electrochemical performances of Mn²⁺/Zn²⁺ HB in 2 M ZnSO₄ aqueous electrolyte with 1 M MnSO₄ as additive. a) GCD curves at different current densities, b) CV curves at different scan rates. c) Rate performance and d) the long-term cycling performance of Mn²⁺/Zn²⁺ HB.

scan rate increasing, a broadened shape and an increased area of CV peaks without obvious polarization are observed. As a comparison, an alkaline Zn–Mn battery was also assembled with the same electrode and 6 M KOH as electrolyte (Figure S16a, Supporting Information). It exhibits the peak specific area capacity of only 0.37 mAh cm⁻² and a narrower voltage window of 0.5–1.9 V based on electrochemical conversion mechanism between MnO₂ and Mn(OH)₂ (Figure S16b, Supporting Information). In addition, serious corrosion originated from the reaction of Zn²⁺ + 2OH⁻ → Zn(OH)₂ on Zn anode in alkaline electrolyte resulted in a relatively low efficiency of 96%, which is reflected by the changes in optical images of Zn foil after cycling (inset in Figure S16c in the Supporting Information). The unstable cycle performance with a capacity retention of 66.9% after 400 cycles is observed. In terms of the rate performance, Mn²⁺/Zn²⁺ HB delivered the capacities of 0.96, 0.75, 0.62, 0.46, 0.35, 0.28, 0.22, 0.17 mA h cm⁻² at different current densities of 1, 1.5, 2, 2.5, 3, 3.5, 4, and 5 mA cm⁻², respectively (Figure 4c).

When the rate was shifted back to 1 mA cm⁻², the capacity recovered to 0.90 mAh cm⁻², showing a strong tolerance to the high-speed reaction. Moreover, benefiting from the ultrastable Zn-CNTs anode and highly reversible Mn²⁺ deposition mechanism, when the Mn²⁺/Zn²⁺ HB is galvanostatically charged/discharged at 5 mA cm⁻² to investigate the long-term cycle stability (Figure 4d). Benefiting from the ultrastable Zn-CNTs anode and highly reversible Mn²⁺ deposition mechanism, the Mn²⁺/Zn²⁺ HB exhibits ultrastable cycle performance almost without decay after 11 000 cycles. To the best of our knowledge, it is the longest cycle life in all the AZBs ever reported, even exceeding most of energy storage devices (Table S1, Supporting Information).

2.4. Charge Storage Mechanism of Mn²⁺/Zn²⁺ HB

The ex situ SEM, TEM, XRD, Raman, and XPS measurements of polyester-CNTs@MnO₂ cathode were conducted

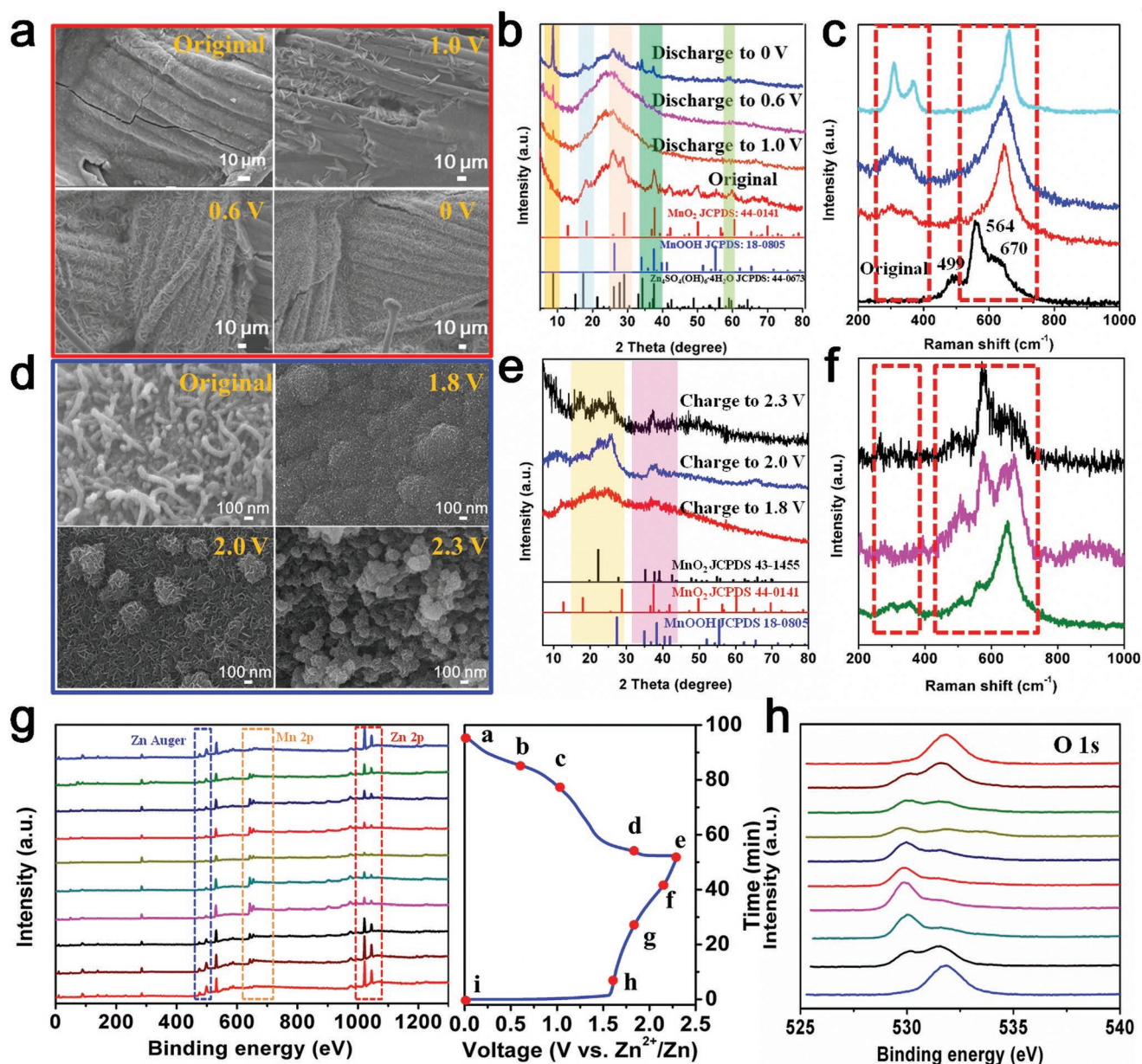
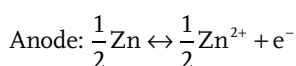
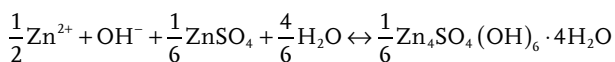


Figure 5. a) SEM images, b) ex situ XRD, and c) ex situ Raman results of polyester-CNTs@MnO₂ cathode during the discharge process from 1.0 to 0 V. d) Ex situ SEM images, e) ex situ XRD, and f) ex situ Raman results of polyester-CNTs@MnO₂ cathode during the charging process from 1.8 to 2.3 V. g) XPS full curves and h) O 1s spectra of polyester-CNTs@MnO₂ cathode at different conditions.

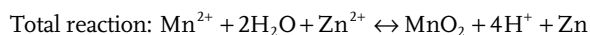
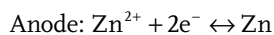
to investigate the charge storage mechanism of Mn²⁺/Zn²⁺ HB. During the about 1.2–1.8 V, the XRD and XPS results of ZnMn₂O₄ are observed, which is consistent with the Zn²⁺ insertion mechanism ($\text{Zn}^{2+} + 2\text{e}^- + 2\text{MnO}_2 \leftrightarrow \text{ZnMn}_2\text{O}_4$) at discharge condition (Figure S17, Supporting Information).^[24] As being discharged to about 1–0 V which is related to the conversion reaction of MnO₂, as shown in Figure 5a, the obvious nanosheets can be clearly observed and the corresponding ex situ XRD results (Figure 5b) indicate that the emerging characteristic peaks with increased intensity located at 8–9°, 25–30°, and 32–38° match well with MnOOH and Zn₄SO₄(OH)₆·4H₂O (JCPDS: 44–0673). The TEM, SAED, HRTEM, and the corresponding EDS mapping images further demonstrate the

existence of MnOOH and Zn₄SO₄(OH)₆·4H₂O (Figures S18 and 19, Supporting Information). The formation process of flake-like Zn₄SO₄(OH)₆·4H₂O is the same as that ever reported by Liu and co-workers that MnO₂ reacts with a proton from water to form MnOOH.^[20] After H⁺ reacts with MnO₂, the sequent OH⁻ ions react with ZnSO₄ and H₂O in the aqueous electrolyte to form large flake-like Zn₄SO₄(OH)₆·4H₂O on the electrode and reach a neutral charge in the system. The ex situ Raman results show an emerging pair of high-intensity peaks while discharging to 0 V and the absorption peaks at around 325/375 and 670 cm⁻¹ (Figure 5c), which can be ascribed to Zn–O and Mn–O vibrations originated from Zn₄SO₄(OH)₆·4H₂O and ZnMn₂O₄, respectively.^[25] The above results are also supported

by the emerging strong Zn Auger and Zn 3s characteristic peaks due to $\text{Zn}_4\text{SO}_4(\text{OH})_6 \cdot 4\text{H}_2\text{O}$,^[26] and the increased Mn^{3+} species (MnOOH) are well supported (Figure S20, Supporting Information).^[27] Hence, the reaction process can be described as below



During the charge process from about 1.8 to 2.3 V, the ex situ SEM images show the obvious deposition product on the surface of cathode (Figure 5d; Figure S21, Supporting Information), indicating that a new mechanism of Mn^{2+} deposition occurs in this $\text{Mn}^{2+}/\text{Zn}^{2+}$ HB system. TEM and the corresponding ex situ XRD (Figure 5e; Figure S22, Supporting Information) demonstrates that two types of MnO_2 with different crystal structures are deposited. The chain-structure MnO_2 (Crystal system: Orthorhombic, with the space group of Pnma, space group number of 62; $a = 9.26 \text{ \AA}$, $b = 2.86 \text{ \AA}$, $c = 4.51 \text{ \AA}$, $\alpha = \beta = \gamma = 90^\circ$) is different from tunnel $\alpha\text{-MnO}_2$ (Figure S23, Supporting Information). Herein, the deposition mechanism can be described as below



The ex situ Raman spectra show the weakened Zn–O ($325/375 \text{ cm}^{-2}$) and Mn–O (670 cm^{-2}) vibrations when charged to 1.8 V due to the extraction of Zn^{2+} from MnO_2 . It was consistent with ex situ XPS results that the obviously increased ratio of $\text{Mn}^{4+}/\text{Mn}^{3+}$ species can be observed at 1.8 V (Figure S20b, Supporting Information). As the charge process proceeds, the ex situ Raman spectra indicate the increasing intensity of characteristic peaks located at 499 and 564 cm^{-1} , indicating the existence of MnO_2 deposition (Figure 5f). Furthermore, the inductively coupled plasma atomic emission spectrometer (ICP-AES) display declining value of Mn/Zn element ratio at 2.3 V in electrolyte due to the deposition/dissolution process of MnO_2 (Figures S24 and S25, Supporting Information). As shown in Figure 5g, the ex situ XPS analyses in marked area display the periodic change of Zn Auger, Mn 2p, and Zn 2p characteristic peaks. In general, the significantly weakened peaks of Zn Auger and Zn 2p in polyester-CNTs@ MnO_2 cathode during the charge processes are due to the dissolved $\text{Zn}_4\text{SO}_4(\text{OH})_6 \cdot 4\text{H}_2\text{O}$ and Zn^{2+} extraction from MnO_2 . In particular, the $\text{Zn}_4\text{SO}_4(\text{OH})_6 \cdot 4\text{H}_2\text{O}$ nanosheets uniformly grow on the surface of electrode when the cathode was discharged to 0 V, resulting in a low intensity peaks of Mn 2p due to the limited depth of detection.^[28] Moreover, the O 1s spectra show the obvious change in Figure 5h during the charge-discharge process. It is caused by the valence change

of Mn species, which is reflected by the peak strength of Mn–O–Mn (MnO_2), Mn–OH (MnOOH), and H–OH in Figure S26 in the Supporting Information. The highest intensity of Mn–O–Mn can be observed at 2.3 V which is due to MnO_2 deposition. Correspondingly, the peak intensity of Mn–OH is highest when discharged to 0 V due to MnOOH . The increasing peak of H–OH is caused by crystal water from $\text{Zn}_4\text{SO}_4(\text{OH})_6 \cdot 4\text{H}_2\text{O}$ or absorbed H_2O .^[29] As a result, this work proposed a new hybrid reaction mechanism in AZBs to widen the voltage window by using a mixed electrolyte of ZnSO_4 and MnSO_4 which involves the oxidation deposition of Mn^{2+} from the electrolyte. It provides another simple way different from that using the “water in salt” electrolyte to widen the voltage window in aqueous battery systems.^[30]

3. Conclusion

In conclusion, we firstly fabricated a dendrite-free Zn anode by CNTs protective layer coating and demonstrated the positive effect of CNTs layer in the inhibition of Zn dendrite and regulation of side reactions by the ex situ XRD and DFT calculations. In addition, a flexible bind-free integrated MnO_2 electrode was produced based on insulating low-cost polyester cloth. After detailed characterizations and balanced evaluations, we have successfully assembled a novel $\text{Mn}^{2+}/\text{Zn}^{2+}$ HB with a wide voltage window (0–2.3 V) based on a new and highly reversible mechanism of $\text{Mn}^{2+}/\text{MnO}_2$ deposition/dissolution, which is much broader than all the AZBs in mild electrolyte ever reported to the best of our knowledge. Meanwhile, it can achieve an ultrastable performance after over 11 000 cycles without decay, high capacity of 0.96 mAh cm^{-2} . Our research successfully develops the $\text{Mn}^{2+}/\text{Zn}^{2+}$ HB in a mild aqueous electrolyte battery system and brings great inspiration in developing the high-performance AZBs.

4. Experimental Section

Synthesis of CNTs Ink: 2.5 g commercial CNTs powers (prepared by CVD; purity: 96 wt%; 10–30 nm in diameter; Suzhou TANFENG graphene Tech Co., Ltd.) and 1 g PVP (K29–32) were added into 25 mL alcohol and 25 mL deionized water (DI water) by ultrasonication treatment for 1 h to form a uniformly dispersed slurry. As a contrast, the CNTs ink without PVP as surfactant was also configured by the same method.

Synthesis of Zn-CNTs Anode: Prior to the synthesis procedure, the Zn foil was polished to remove the oxide layer. A piece of Zn foil was then dipped the CNT ink and taken out to dry in a vacuum oven at 50°C for 3 h. Finally, the dried Zn-CNTs was rinsed several times with DI water, alcohol to remove the residual surfactant and dried in an oven at 70°C .

Synthesis of Polyester-CNTs Conductive Substrate: The typical process was carried out by the following steps. First, a piece of polyester cloth was cut off from clothes ($5 \times 3 \text{ cm}^2$) and soaked in concentrated HNO_3 for 5 h. Then washed with DI water and alcohol several times to remove the residual acid; and then the polyester cloth was dried in a vacuum oven at 70°C . Next, the prewashed polyester cloth was dipped into the CNTs ink and dried in vacuum at 70°C overnight. Finally, the dried polyester-CNTs conductive substrate was rinsed several times with DI water, alcohol to remove the residual surfactant and dried in an oven at 70°C . The mass loading is 1.9 mg cm^{-2} .

Synthesis of Polyester-CNTs@ MnO_2 Cathode: The MnO_2 was in situ grown on the polyester-CNTs via a self-sacrifice reaction process, which

can be interpreted the reaction as $4\text{KMnO}_4 + 3\text{C} + \text{H}_2\text{O} \rightarrow 4\text{MnO}_2 + \text{K}_2\text{CO}_3 + 2\text{KHCO}_3$.^[31] Simply, the 0.5 g KMnO_4 was dissolved in 50 mL DI water under constant magnetic stirring for a few minutes to form a dark purple solution. The solution containing a piece of pretreated polyester-CNTs substrate was then transferred to a Teflon-lined stainless-steel autoclave (100 mL). The autoclave was sealed and maintained at 120 °C for 0.5, 1, 1.5, and 2 h, respectively. And then it was cooled to room temperature. After the sample was taken out, it was rinsed several times with DI water and dried in an oven at 70 °C to obtain polyester-CNTs@ MnO_2 .

Materials Characterization: To observe the morphology, SEM (and EDS)/TEM (and HRTEM) were performed with JEOL JSM-7100F scanning electron microscope and JEM-2100F/Titan G2 60–300 transmission electron microscope. X-ray diffractometer characterizations were carried out with a D8 Discover X-ray diffractometer with non-monochromated $\text{Cu K}\alpha$ X-ray source ($\lambda = 1.054056 \text{ \AA}$). The ex situ electrochemistry-Raman measurements were recorded using a HORIBA HR EVO Raman system (633 nm laser). XPS measurements were performed using a VG MultiLab 2000 instrument. The contact angles of water drops deposited were measured using a contact angle meter (SL150, Kino industrial co., LTD, USA). The strength test were calculated by electromechanical universal testing machine (Mts Systems Co., LTD, China). The element contents were determined by ICP-AES on a PLASMA 300 apparatus, and its accuracy is 0.1%. EDS measurement was performed using an Oxford EDS IE250. The mass of the electrodes was also recorded by an AX/MX/UMX Balance (METTLER TOLEDO, maximum = 5.1 g; delta = 0.001 mg).

Theoretical Computation of DFT and Model: The binding energies of O and S with Zn (202) plane or CNTs are theoretically calculated by DFT, which is implemented by DMol3 module in Materials Studio software.^[32] Zn (202) lattice plane was constructed according to the XRD pattern of Zn metal, which shows the highest intensity of reflection peak at (202) plane. The CNT model with a pyrrolic N atom and an O atom was designed in correspondence with the XPS tests. During the geometry optimization of structures, the Perdew–Burke–Ernzerh (PBE) generalized gradient approximation functional has been employed.^[33] Besides, van der Waals interaction has been considered and corrected by Grimme method.^[34] The electronic self-consistent field tolerance was set as 1×10^{-6} eV per atom, while the energy tolerance of geometry optimization was set as 1.0×10^{-5} eV per atom. The binding energies are calculated by minus the energies of the single parts from complex adsorption structure, which can be described by beneath equation

$$E_b = E(\text{Absorbate/Absorbant}) - E(\text{Absorbate}) - E(\text{Absorbant})$$

The energy of a single O atom is equal to half of an O_2 molecular, and a single S is one-eighth of S_8 molecular. A single Zn atom can be treated as one atom of Zn metal.

Intensity Calculation of Tension: The intensity of tension is calculated according to the formula: $\sigma_t = p/(b \times d)$, where σ_t is tensile strength (MPa); p is tension load (N); b is width of sample (mm); d is the thickness of sample (mm).

Electrochemical Characterization: Zinc foil or Zn-CNTs, filter paper, 2 M Zn zinc sulfate with 0.2 M manganese sulfate additive solution were employed as the anode, separator, and electrolyte, respectively. A CR2016-type coin symmetrical cell Zn-CNTs (or Zn foil) | 2 M ZnSO_4 + 0.2 M MnSO_4 | Zn-CNTs (or Zn foil) was assembled in air. The cells underwent galvanostatic charging-discharging cycling at a current density of 0.5 mA cm^{-2} and a total capacity of 0.15 mAh cm^{-2} to evaluate the stripping/plating behavior and cycling stability of Zn-CNTs or Zn foils with a LAND battery testing system (CT2001A). The EIS were recorded on a 760E Electrochemical Workstation (CH Instruments, China) with a frequency range from 100 kHz to 0.01 Hz. A Hg/HgO and a platinum foil ($2 \times 2 \text{ cm}^2$) were employed as reference and counter electrodes, respectively. The measurements were carried out at room temperature in a three-electrode electrochemical cell with a bare or a CNTs coated Zn foil as the work electrode. The $\text{Mn}^{2+}/\text{Zn}^{2+}$ HB system was fabricated with polyester-CNTs@ MnO_2 cathode and Zn-CNTs anode. GCD and

CV curves and electrochemical impedance spectroscopy (EIS, 100 kHz to 0.01 Hz, 5 mV amplitude) are conducted by utilizing an 760E Electrochemical Workstation (CH Instruments, China) testing system with two-electrode configuration at room temperature.

Supporting Information

Supporting Information is available from the Wiley Online Library or from the author.

Acknowledgements

This work was supported by the National Natural Science Fund for Distinguished Young Scholars (51425204), the National Natural Science Foundation of China (51521001, 51302203, 51832004), the National Key Research and Development Program of China (2016YFA0202603), the Programme of Introducing Talents of Discipline to Universities (B17034), the Yellow Crane Talent (Science & Technology) Program of Wuhan City and the National Basic Research Program of China (2013CB934103).

Conflict of Interest

The authors declare no conflict of interest.

Keywords

11000-cycle lifespan, 2.3 V voltage window, dendrite-free, $\text{Mn}^{2+}/\text{Zn}^{2+}$ hybrid batteries

Received: May 4, 2019

Revised: June 2, 2019

Published online:

- [1] a) J. Rugolo, M. J. Aziz, *Energy Environ. Sci.* **2012**, *5*, 7151; b) M. Armand, J.-M. Tarascon, *Nature* **2008**, *451*, 652; c) P. Simon, Y. Gogotsi, *Nat. Mater.* **2008**, *7*, 845; d) H. K. Bruce Dunn, J.-M. Tarascon, *Science* **2011**, *334*, 928.
- [2] a) L. Xu, S. Tang, Y. Cheng, K. Wang, J. Liang, C. Liu, Y.-C. Cao, F. Wei, L. Mai, *Joule* **2018**, *2*, 1991; b) H. Pan, Y.-S. Hu, L. Chen, *Energy Environ. Sci.* **2013**, *6*, 2338; c) Z. Yi, Z. Wang, Y. Cheng, L. Wang, *Energy Environ. Mater.* **2018**, *1*, 132.
- [3] a) H. Li, C. Han, Y. Huang, Y. Huang, M. Zhu, Z. Pei, Q. Xue, Z. Wang, Z. Liu, Z. Tang, Y. Wang, F. Kang, B. Li, C. Zhi, *Energy Environ. Sci.* **2018**, *11*, 941; b) D. Ba, Y. Li, Y. Sun, Z. Guo, J. Liu, *Sci. China Mater.* **2019**, *62*, 487.
- [4] a) J. Huang, Z. Guo, Y. Ma, D. Bin, Y. Wang, Y. Xia, *Small Methods* **2019**, *3*, 1800272; b) J. Qiu, M. Zhao, Q. Zhao, Y. Xu, L. Zhang, X. Lu, H. Xue, H. Pang, *Sci. China Mater.* **2017**, *60*, 577; c) X. Wu, A. Markir, Y. Xu, C. Zhang, D. P. Leonard, W. Shin, X. Ji, *Adv. Funct. Mater.* **2019**, *29*, 1900911; d) S. Gheyhani, Y. Liang, F. Wu, Y. Jing, H. Dong, K. K. Rao, X. Chi, F. Fang, Y. Yao, *Adv. Sci.* **2017**, *4*, 1700465; e) C. Yang, X. Ji, X. Fan, T. Gao, L. Suo, F. Wang, W. Sun, J. Chen, L. Chen, F. Han, L. Miao, K. Xu, K. Gerasopoulos, C. Wang, *Adv. Mater.* **2017**, *29*, 1701972; f) Y. Li, Q. An, Y. Cheng, Y. Liang, Y. Ren, C.-J. Sun, H. Dong, Z. Tang, G. Li, Y. Yao, *Nano Energy* **2017**, *34*, 188.
- [5] L. Ma, S. Chen, H. Li, Z. Ruan, Z. Tang, Z. Liu, Z. Wang, Y. Huang, Z. Pei, J. A. Zapien, C. Zhi, *Energy Environ. Sci.* **2018**, *11*, 2521.

- [6] A. Konarov, N. Voronina, J. H. Jo, Z. Bakenov, Y.-K. Sun, S.-T. Myung, *ACS Energy Lett.* **2018**, *3*, 2620.
- [7] a) M. Li, J. Meng, Q. Li, M. Huang, X. Liu, K. A. Owusu, Z. Liu, L. Mai, *Adv. Funct. Mater.* **2018**, *28*, 1802016; b) C. Li, Q. Zhang, J. Sun, T. Li, S. E. Z. Zhu, B. He, Z. Zhou, Q. Li, Y. Yao, *ACS Energy Lett.* **2018**, *3*, 2761.
- [8] J. Pan, Y. Y. Xu, H. Yang, Z. Dong, H. Liu, B. Y. Xia, *Adv. Sci.* **2018**, *5*, 1700691.
- [9] G. Li, Z. Yang, Y. Jiang, C. Jin, W. Huang, X. Ding, Y. Huang, *Nano Energy* **2016**, *25*, 211.
- [10] J. F. Parker, C. N. Chervin, E. S. Nelson, D. R. Rolison, J. W. Long, *Energy Environ. Sci.* **2014**, *7*, 1117.
- [11] a) M. Song, H. Tan, D. Chao, H. J. Fan, *Adv. Funct. Mater.* **2018**, *28*, 1802564; b) N. Zhang, Y. Dong, M. Jia, X. Bian, Y. Wang, M. Qiu, J. Xu, Y. Liu, L. Jiao, F. Cheng, *ACS Energy Lett.* **2018**, *3*, 1366; c) M. Yan, P. He, Y. Chen, S. Wang, Q. Wei, K. Zhao, X. Xu, Q. An, Y. Shuang, Y. Shao, K. T. Mueller, L. Mai, J. Liu, J. Yang, *Adv. Mater.* **2018**, *30*, 1703725. d) J. Huang, Z. Wang, M. Hou, X. Dong, Y. Liu, Y. Wang, Y. Xia, *Nat. Commun.* **2018**, *9*, 2906.
- [12] C. N. Chervin, J. F. Parker, I. R. Pala, M. Machler, M. F. Burz, J. W. Long, D. R. Rolison, *Science* **2017**, *356*, 415.
- [13] N. Zhang, F. Cheng, Y. Liu, Q. Zhao, K. Lei, C. Chen, X. Liu, J. Chen, *J. Am. Chem. Soc.* **2016**, *138*, 12894.
- [14] L. Kang, M. Cui, F. Jiang, Y. Gao, H. Luo, J. Liu, W. Liang, C. Zhi, *Adv. Energy Mater.* **2018**, *8*, 1801090.
- [15] D. Chao, C. R. Zhu, M. Song, P. Liang, X. Zhang, N. H. Tiep, H. Zhao, J. Wang, R. Wang, H. Zhang, H. J. Fan, *Adv. Mater.* **2018**, *30*, 1803181.
- [16] W. Chen, G. Li, A. Pei, Y. Li, L. Liao, H. Wang, J. Wan, Z. Liang, G. Chen, H. Zhang, J. Wang, Y. Cui, *Nat. Energy* **2018**, *3*, 428.
- [17] J. C. M. J. L. Salager, R. S. Schechter, W. H. Wade, M. Spe-Aime, E. Vasquez, *Soc. Pet. Eng. J.* **1979**, *19*, 107.
- [18] J. K. Seung Woo Lee, S. Chen, P. T. Hammond, Y. Shao-Horn, *ACS Nano* **2010**, *4*, 3889.
- [19] B. Wu, G. Zhang, M. Yan, T. Xiong, P. He, L. He, X. Xu, L. Mai, *Small* **2018**, *14*, 1703850.
- [20] H. Pan, Y. Shao, P. Yan, Y. Cheng, K. S. Han, Z. Nie, C. Wang, J. Yang, X. Li, P. Bhattacharya, K. T. Mueller, J. Liu, *Nat. Energy* **2016**, *1*, 16039.
- [21] X. Wang, F. Wang, L. Wang, M. Li, Y. Wang, B. Chen, Y. Zhu, L. Fu, L. Zha, L. Zhang, Y. Wu, W. Huang, *Adv. Mater.* **2016**, *28*, 4904.
- [22] F. G. Cottrell, *J. Phys. Chem.* **1899**, *4*, 637.
- [23] W. Sun, F. Wang, S. Hou, C. Yang, X. Fan, Z. Ma, T. Gao, F. Han, R. Hu, M. Zhu, C. Wang, *J. Am. Chem. Soc.* **2017**, *139*, 9775.
- [24] N. Zhang, F. Cheng, J. Liu, L. Wang, X. Long, X. Liu, F. Li, J. Chen, *Nat. Commun.* **2017**, *8*, 405.
- [25] a) N. Hammouda, H. Chadli, G. Guillemot, K. Belmokre, *Adv. Chem. Eng. Sci.* **2011**, *01*, 51; b) C.-C. Hu, Y.-T. Wu, K.-H. Chang, *Chem. Mater.* **2008**, *20*, 2890.
- [26] a) J. Duchoslav, R. Steinberger, M. Arndt, D. Stifter, *Corros. Sci.* **2014**, *82*, 356; b) B. R. Strohmeier, D. M. Hercules, *J. Catal.* **1984**, *86*, 266.
- [27] N. Jabeen, A. Hussain, Q. Xia, S. Sun, J. Zhu, H. Xia, *Adv. Mater.* **2017**, *29*, 1700804.
- [28] a) F. Bensebaa, F. Zavaliche, P. L'Ecuyer, R. W. Cochrane, T. Veres, *J. Colloid Interface Sci.* **2004**, *277*, 104; b) L. Xu, M. Salmeron, *Langmuir* **1998**, *14*, 5841.
- [29] G. Fang, C. Zhu, M. Chen, J. Zhou, B. Tang, X. Cao, X. Zheng, A. Pan, S. Liang, *Adv. Funct. Mater.* **2019**, *29*, 1808375.
- [30] L. Suo, O. Borodin, W. Sun, X. Fan, C. Yang, F. Wang, T. Gao, Z. Ma, M. Schroeder, A. von Cresce, S. M. Russell, M. Armand, A. Angell, K. Xu, C. Wang, *Angew. Chem., Int. Ed.* **2016**, *55*, 7136.
- [31] X. Jin, W. Zhou, S. Zhang, G. Z. Chen, *Small* **2007**, *3*, 1513.
- [32] a) B. Delley, *J. Chem. Phys.* **1990**, *92*, 508; b) B. Delley, *J. Chem. Phys.* **2000**, *113*, 7756.
- [33] J. P. Perdew, K. Burke, M. Ernzerhof, *Phys. Rev. Lett.* **1996**, *77*, 3865.
- [34] S. Grimme, J. Antony, S. Ehrlich, H. Krieg, *J. Chem. Phys.* **2010**, *132*, 154104.